Direct Measurements of the Convective Recycling of the Upper Troposphere

Timothy H. Bertram[1], Anne E. Perring[1], Paul J. Wooldridge[1], John D. Crounse[3], Alan J. Kwan[4], Paul O. Wennberg[4,5], Eric Scheuer[6], Jack Dibb[6], Melody Avery[7], Glen Sachse[7], Stephanie A. Vay[7], James H. Crawford[7], Cameron S. McNaughton[8], Antony Clarke[8], Kenneth E. Pickering[9], Henry Fuelberg[10], Greg Huey[11], Donald R. Blake[12], Hanwant B. Singh[13], Samuel R. Hall[14], Richard E. Shetter[14], Alan Fried[14], Brian G. Heikes[15], and Ronald C. Cohen[1,2]

[1]Department of Chemistry; University of California, Berkeley
[2]Department of Earth and Planetary Science; University of California, Berkeley
[3]Division of Chemistry and Chemical Engineering; California Institute of Technology
[4]Division of Engineering and Applied Science; California Institute of Technology
[5]Division of Geological and Planetary Sciences; California Institute of Technology
[6]Institute for the Study of Earth, Oceans, and Space; University of New Hampshire
[7]NASA Langley Research Center; Hampton, VA
[8]School of Ocean and Earth Science Technology; University of Hawaii, Manoa
[9]Department of Atmospheric and Oceanic Science; University of Maryland
[10]Department of Meteorology; Florida State University
[11]School of Earth and Atmospheric Sciences; Georgia Institute of Technology
[12]Department of Chemistry; University of California, Irvine
[13]NASA Ames Research Center; Moffett Field, CA
[14]The National Center for Atmospheric Research; Boulder, CO
[15]Graduate School of Oceanography; University of Rhode Island

We present a statistical representation of the aggregate effects of deep convection on the chemistry and dynamics of the Upper Troposphere (UT) based on direct aircraft observations of the chemical composition of the UT over the Eastern United States and Canada during summer. These measurements provide new and unique observational constraints on the chemistry occurring downwind of convection and the rate at which air in the UT is recycled, previously only the province of model analyses. These results provide quantitative measures that can be used to evaluate global climate and chemistry models.

Deep convection is a highly efficient mechanism for the vertical transport of air from near the Earth's surface (0-2 km) to the Upper Troposphere (UT) (6-12 km) (*1-5*). Typical convective storms have spatial scales of tens of kilometers and vertical velocities as large as 15 m sec^{-1} (*6*), making their local influence in the UT extremely strong. The rapid upward flow is balanced by much slower descending flow that occurs over a larger spatial scale (*7*). Convection is also associated with lightning a significant source of NO_x ($NO_x \equiv NO + NO_2$) in the UT (*8, 9*). The source strength and spatial distribution of lightning NO_x emissions are not well known, with estimates ranging from 2-20 Tg(N) yr^{-1} for the global average (*10*), compared to 25 Tg(N) yr^{-1} from fossil fuel combustion (*11*). Although there have been a number of case studies of the chemical effects of individual storms (*12*), studies of the aggregate effects of convection on the chemical composition and radiative forcing of the UT have been largely the province of modeling and theory (*13, 14*). Here we describe measurements that provide a direct link between an observable property and the ensemble of convective events.

The chemical and radiative consequences of convection and lightning are known to be large (*2, 3, 15*). Upper tropospheric O_3, either transported directly from the boundary layer via convection or formed in situ following detrainment of convectively lofted O_3 precursors (NO_x, odd hydrogen radicals (HO_x) and hydrocarbons) in the outflow region, directly impacts climate through a positive radiative forcing (*15*). Additionally, deep convection accounts for a significant fraction of the net flux of moisture from near the Earth's surface to the UT (*16*). Thus, the rate at which the UT is turned over by

convection has important implications on the hydrological cycle and the magnitude of the water vapor feedback on global temperature (*17*).

In this study we describe a method for calculating the time air spends in the upper troposphere following convection from in situ measurements of the chemical composition of the UT and discuss the chemistry occurring in the outflow region as a function of time since convection. We use measurements of NO_2 (*18, 19*) (NO_x is calculated from NO_2, O_3, HO_2 and photolysis rates), HNO_3 (*20, 21*), OH and HO_2 (*22*), O_3 (*23*), aerosol number density (*24*), actinic flux (*25*), CO (*26*) and CO_2 (*27*) obtained during the Intercontinental Chemical Transport Experiment – North America (INTEX-NA) aboard the NASA DC-8 (*28*). Measurements were made at altitudes between the surface and 12.5 km, over a wide area of the US and Canada, west of 40º W and between 30 and 50º N. There were a large number of vertical profiles allowing a reasonably unbiased statistical sampling of air over this region during July and August of 2004.

We use the deviation of the observed NO_x to HNO_3 ratio from steady-state as an indicator of convective influence. The NO_x to HNO_3 ratio is reset to near infinity in moist convection as a result of preferential wet scavenging of HNO_3 relative to NO_x (i.e., the Henry's Law Constant for HNO_3 is ~ 10^8 times larger than for NO_x) (*29*). Further, lightning initiated NO_x production, often coincident with convection, dramatically enhances NO_x in the outflow region. The coupling of these processes makes the NO_x to HNO_3 ratio in the UT an effective indicator of convective influence, where $NO_x/HNO_3 >> 1$ is indicative of recent cloud outflow (*30, 31*). In the days following convection, the

ratio decays toward steady-state providing a chemical clock that marks the time an air-mass has spent in the UT following convection (*32*). A number of previous studies have used species which have no upper tropospheric source (e.g. CH_3I) (*33*), or alternative chemical ratios to provide estimates of age of air in the UT (*34, 35*). Our study is unique because of the availability of high time resolution NO_2, OH and HNO_3 measurements that allow us to build a much more extensive data set than previous studies. After the initial turbulent mixing in the near field of the convection, mixing is slow, thus the time evolution of NO_x/HNO_3 following convection depends largely on the partitioning of NO_x (between NO and NO_2), the concentration of OH and the actinic flux.

Reactive Nitrogen Partitioning in the UT

The only significant chemical sinks of UT NO_x are reaction with OH to produce HNO_3 (Equation 1) and nighttime loss through NO_3 (Equation 2a-b) followed by hydrolysis of N_2O_5 to produce HNO_3 (*36*). NO_x is regenerated by nitric acid photolysis (and subsequent NO_3 photolysis to NO_2) and reaction of OH with HNO_3 (Equations 3 and 4).

$$NO_2 + OH \rightarrow HNO_3 \quad (1)$$

$$NO_2 + O_3 \rightarrow NO_3 + O_2 \quad (2a)$$

$$NO_3 + NO_2 \rightarrow N_2O_5 \quad (2b)$$

$$HNO_3 \xrightarrow{h\nu} OH + NO_2 \quad (3)$$

$$HNO_3 + OH \rightarrow NO_3 + H_2O \quad (4)$$

Including the altitude dependent rain-out rate for HNO_3 ($k_{rain\text{-}out}$) as derived by Giorgi and Chameides (*37*), the expected steady-state NO_x/HNO_3 is:

$$\left(\frac{[NO_x]}{[HNO_3]}\right)_{Steady-State} = \frac{J_{HNO_3} + k_{HNO_3+OH}[OH] + k_{HNO_3\ rainout}}{\left(k_{NO_2+OH}[OH] + 2k_{N_2O_5+H_2O}\frac{[N_2O_5]}{[NO_2]}\right)x\left(\frac{[NO_2]}{[NO_x]}\right)} \quad (3)$$

Our observations show the NO_x to HNO_3 ratio to be much higher than the ratio described by equation 3 at altitudes greater than 6 km (c.f. Fig. 2). The difference between the observed ratio and that predicted by equation 3 grows with altitude, reaching a maximum at 10 km. Previous observations of NO_x and HNO_3 (either measured directly or calculated from observations of NO_x, PAN and NO_y) have shown the NO_x/HNO_3 ratio to be significantly larger than the steady-state prediction in the UT (*30, 31, 38-42*). This has been shown to be primarily a result of convection and lightning reinitializing the system before steady-state is achieved (*30, 31*). Although a series of other hypotheses have been put forth (*40-42*), we (like Jaegle et al.) find no evidence for a mechanism other than convection responsible for holding NO_x/HNO_3 out of steady-state in the UT.

Chemical Signatures of Convection

Fig. 3 depicts one of many convectively influenced air-masses sampled in the UT during INTEX-NA. Three distinct convective events (40–80 km wide) are identified by enhancements in NO_x/HNO_3 in Fig. 3a. Coincident enhancements are present in SO_2, an indicator of a recent boundary layer source for this air, and Ultra-fine Cloud Condensation Nuclei (UCN) ($3 \leq D_p \leq 10$ nm), an indicator of cloud detrainment (Fig. 3b) (*43, 44*). Sharp decreases in CO_2 also indicate the convective lofting of boundary layer air depleted in CO_2, a result of photosynthetic activity (Fig. 3c) (*44*). Enhancements in CO, CH_2O and various hydrocarbons, relative to the surrounding UT

air, were also observed in these plumes, further indicating that these parcels originate from the Planetary Boundary Layer (PBL). Backward air trajectories, initialized along the flight track, coupled to the spatial and temporal distribution of cloud-to-ground lightning strikes, indicate that the sampled air-mass was recently influenced by lightning approximately one day prior to DC-8 sampling (c.f. Fig. 3 bottom panel) (*45*). Such features with high NO_x/HNO_3 were observed throughout the UT during INTEX-NA.

To assess the extent to which the UT over the Eastern U.S. and Canada during the summer of 2004 was influenced by convection and describe the chemical evolution of convective outflow, we use a constrained time-dependent photo-chemical box model to map the observed NO_x/HNO_3 to the time since the ratio was last reinitialized. The model is described in the supplemental information included with this article. It is initialized with observations at 1km vertical intervals from 6 to 12 km. The derived timing indicator for the convectively influenced air sampled on 11 August 2006 is shown in Fig. 3d. The properties of the ensemble of our measurements are shown in Figs. 4-6.

The aerosol size distribution provides an independent indicator of air recently detrained from clouds. Cloud-processed air is depleted of aerosol surface area permitting new particle formation in the outflow region (*43, 44*). Fig. 4a depicts the fraction of condensation nuclei found in the 3-10 nm bin as a function of time since convective influence. The fraction of particles in this ultra-fine mode is largest during the first few days confirming that the NO_x to HNO_3 ratio, and the timing indicator derived from it, is reinitialized in the UT by cloud processing. Strong enhancements in CH_3OOH/H_2O_2 (not

shown), also an indicator of recent cloud processing (*33, 46*), were observed during the first two days after cloud processing.

As expected, both elevated NO_x and suppressed HNO_3 are observed at short times (c.f. Figs. 4b-c). Enhancements in NO_x during the first few days is indicative of convection of boundary layer and/or lightning NO_x (*47, 48*). The suppression of HNO_3 at short times is clear indication of HNO_3 scavenging during convection. Fig. 4d confirms that reactive nitrogen ($NO_y \equiv NO_x$ + total peroxy nitrates + HNO_3) is conserved during the chemical processing following convection, a fact which provides further support for the use of NO_x/HNO_3 as a marker representing time since convection.

Chemical Processing in Convective Outflow

Mapping the ensemble of observations made throughout the UT onto the coordinate of time since convection allows us to assess the chemical and dynamical processes occurring following convection, without attempting a Lagrangian convection study. In this analysis we concentrate on the time evolution of CO and O_3.

The time evolution of CO, following detrainment into the UT, is set by the abundance of OH and the rate at which the convective plume entrains air from the background UT (c.f. Fig. 5a). Due to the direct dependence of the chemical clock on HO_x, we constrained both OH and HO_2 to the observations as a function of NO_x and pressure in the time-dependent model used to generate time. As a result, we can iterate the model to determine the proper mixing rate of the convective plume by matching the modeled and

observed time evolution of CO following convection. Using this approach for a series of long lived species (e.g. CO, CH_4, CH_3OH and others), we calculate an average mixing rate of 0.05 ± 0.02 day^{-1} following detrainment into the UT. This is in good agreement with the upper limit of 0.06 - 0.1 day^{-1} determined by Ray et al. from observations of convective plumes observed in the stratosphere during the CRYSTAL-FACE mission (*49*), however it is slower than the 2 day dilution time-scale determined by Wang et al. from observations during the SONEX Experiment (*32*). Since the DC-8 did not routinely sample in the turbulent environment directly surrounding convective outflow, this mixing rate likely reflects diffusive and shear induced mixing subsequent to the initial turbulent mixing occurring during detrainment from the convective system. Entrainment of UT air either during convective lofting or cloud detrainment is discussed in the next section.

The O_3 mixing ratio as a function of time since convection is shown in Fig. 5b. We find that on average, convectively lofted air-masses contain less O_3 than the background UT. This result is consistent with the observed vertical gradient in O_3 observed over the continental US during INTEX-NA, with lower O_3 in the PBL than above (*50*). Rapid changes in the O_3 mixing ratio are observed during the first two days following detrainment, with the observed O_3 15 nmol mol^{-1} above the initial value by the end of day two. The observed rate of increase slows exponentially with an asymptote at long time approaching zero and the O_3 mixing ratio approaching a constant value of 85 nmol mol^{-1}. This is a surprising result, as our model of the O_3 rate of change never approaches zero, but continues to predict a net increase of 3 nmol mol^{-1} O_3 day^{-1} at the end of day five (*51*).

Constraints on the Convective Turnover Rate of the UT

The convective turnover rate of the upper troposphere is critical for accurately describing NO_x, HO_x and O_3 chemistry in the UT (*52*). However, at present there is a paucity of observation based constraints available (either meteorological or chemical) to test the aggregate effects of convection in the current generation of global chemistry and climate models. To determine the convective turnover rate of the UT from the observations presented here, both the extent to which the UT is influenced by convection and the fraction of PBL air in the convectively influenced air-masses must be known with high confidence.

To determine the fraction of PBL air contained in fresh convective outflow, we use observations of insoluble long-lived species made throughout the INTEX-NA campaign over the continent. Assuming that we conducted a statistically unbiased sampling of both the boundary layer and free troposphere during INTEX-NA, we can calculate the fraction of PBL air present in fresh convection (f) through the following equation:

$$[X]_{UT(t=0)} = f\,[X]_{surface} + (1-f)\,[X]_{UT} \qquad (4)$$

where $[X]_{UT\ (t=0)}$ is the mean mixing ratio of species X in fresh convective outflow (as identified using our timing indicator), $[X]_{UT}$ is the mean mixing ratio of species X in the UT (7.5-11.5 km) and $[X]_{surface}$ is the mean mixing ratio of species X between 0-1.5 km. Using observations of CO, CO_2, CH_3OH, CH_4 and C_2H_6 we calculate the fraction of PBL

air in fresh convection to be 0.19 ± 0.05, 0.11 ± 0.03, 0.26 ± 0.05, 0.15 ± 0.05, and 0.34 ± 0.09, respectively. We calculate a weighted average for the fraction of PBL air in convective outflow of 0.17 ± 0.02 by weighting each value by the inverse square of its uncertainty. This implies that convectively lofted PBL air rapidly entrains the surrounding air either during ascent or in the turbulent environment of the detraining flow. These results are consistent with: i.) the observations of Ray et al., who determined the fraction of tropospheric air in convective plumes sampled in the stratosphere to be between 0.1 and 0.4 (*49*), ii.) the observations of Cohan et al., who calculate the fraction of BL air in fresh convection outflow to be between 0.32 and 0.64 from observations of $CHBr_3$, CH_3OOH and CH_3I in fresh convection (*33*) and iii.) the modeling studies of Mullendore et al., who calculate the fraction of PBL air present in the convective outflow region of a supercell storm to be 0.26, 10 hours after storm initialization (*53*).

Fig. 6a shows the normalized frequency distribution of the observed time since convection based on the ratio of NO_x to HNO_3. We find that 54% of the air sampled between 7.5 and 11.5km had been influenced by convection during the past two days. The convective outflow was strongest between 9.5 and 10.5 km, where the fraction of sampled air that is less than two days old exceeds 69%. The vertical distribution presented here is consistent with previous observations and model analyses of convective outflow to the UT from individual storms (*4, 54*) and the vertical distribution of convectively influenced laminae observed in O_3 sonde data from the summer of 2004 over the northeastern U.S. (*55*). The shift toward longer times between 10.5 and 11.5 km suggests that either convective cloud tops on average do not extend higher than 10.5 km

over the mid-latitude during the summer (*56*) or that transport of stratospheric air, rich in HNO_3, contributes to keeping the NO_x to HNO_3 ratio low at altitudes greater than 10.5 km (*57*).

To constrain the turnover rate of the UT from the ensemble statistics generated from our calculated time since convective influence (Fig. 6a), we constructed a two dimensional model of the UT. We assume that it takes 4 days for any individual box to pass through the sampling region and that each box has not been influenced by convection upon entering the sampling window. Every six hours we: i.) represent convection by randomly reinitializing the age of x% of the boxes in the sampling domain to 0 (the value of x is determined by the turnover rate (varied between 0.05 and 0.2 day^{-1}) and the fraction of PBL air contained in fresh convection (assumed to be a constant at 0.17)) and ii.) dilute each box with the mean value of the adjacent 8 boxes at the rate of 0.05 day^{-1}.

Fig. 6b depicts the observed and three calculated normalized frequency distribution of time since convective influence between 7.5 and 11.5 km. The shape of the distribution suggests that UT air sampled during INTEX-NA was largely influenced by convection, and that convectively lofted plumes did not have sufficient time to either mix or age prior to sampling by the DC-8, but instead were transported to the East out of the domain. Frequency distributions of time since convection, using three different convective turnover rates, in the Eastern half of the 2-D UT model analysis (where we sampled most frequently) are also shown in Fig. 6b. Assuming the DC-8 made a statistically unbiased sampling of the continental UT during summer, the best match between the model and

observations would imply a convective turnover rate between 0.1 - 0.2 day^{-1}. However, if we assume the DC-8 had a positive bias toward sampling fresh convection in accordance with Fuelberg et al., our observed frequency distributions are consistent with a convective turnover rate closer to 0.1 day^{-1} (*45, 58*).

For comparison, the model detrainment cloud mass flux between 400 and 200 hPa (approximately 7.2 - 11.8 km based on standard atmosphere) for the INTEX-NA sampling domain (80º - 100ºW for 30º - 35ºN and 70º - 100º W for 35º - 50º N) between July 1st and August 15th 2004 was 0.0085 kg m^{-2} sec^{-1}. This corresponds to a turnover rate of 0.37 day^{-1} (using a column mass of $1.9x10^3$ kg m^{-2} between 7.2 - 11.8 km). As expected, the observed and modeled detrainment rates for the extratropics are slower than in the tropics. For example, Folkins and Martin determine a maximum convective detrainment rate of 0.4 day^{-1} at 12.5 km from calculation of the clear-sky radiative and precipitation induced evaporative cooling rates using a one-dimensional model constrained by observations of temperature and water vapor (*59*).

Conclusions

We present a statistical representation of the aggregate effects of convection on the chemistry and dynamics of the upper troposphere using in situ measurements taken aboard the NASA DC-8 during the summer of 2004 over the Eastern U.S. and Canada. These observations provide a new and unique constraint on: i.) the extent to which convection perturbs the continental UT during summer, ii.) the fraction of boundary layer air present in convective outflow, and iii.) the convective overturn rate of the upper

1 troposphere. In addition, the chemical clock described here defines a coordinate that can
2 be used to assess the chemistry occurring down-wind of convective injection. These
3 direct measures of atmospheric rates present a new opportunity for quantitative tests of
4 model representations of processes governing UT ozone, convection, lightning and their
5 impact on climate.
6

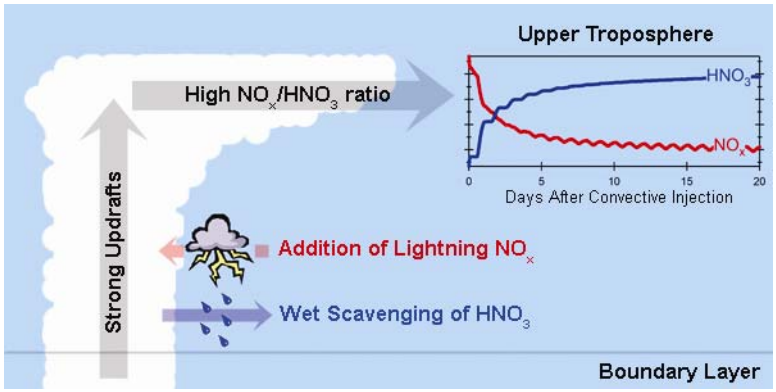

Figure 1: In moist convection, air from near the Earth's Surface is rapidly transported upwards and detrained into the Upper Troposphere. In this process, Nitric Acid (highly soluble) is efficiently scavenged, while NO_x (insoluble) remains. NO_x is dramatically elevated by concurrent lightning NO production, resulting in high NO_x to HNO_3 ratios in the convective outflow region. Following detrainment into the UT, NO_x is converted to HNO_3 by OH during the day and via NO_3/N_2O_5 at night. The chemical evolution of the NO_x/HNO_3 ratio provides a unique indicator of the time a sampled air-mass has been in the UT following convection.

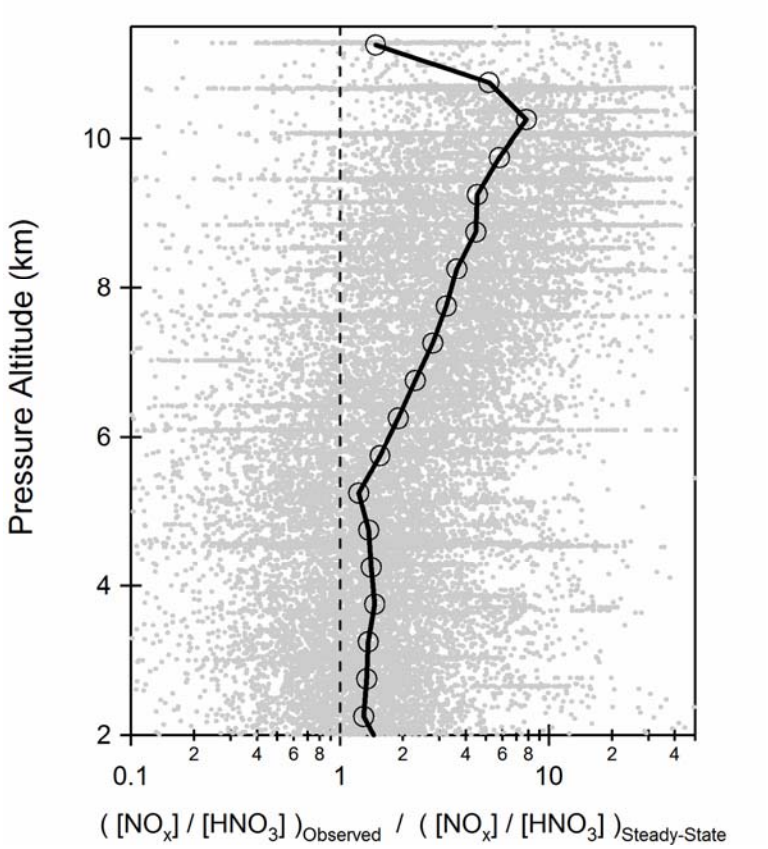

Figure 2: The observed deviation of the NO_x to HNO_3 ratio from steady-state as a function of altitude in the UT. The mean values within 500 m vertical bins are shown with circles (○). The steady-state NO_x to HNO_3 ratio was calculated from measured NO_x, OH and J_{HNO3} and includes the rain out parameterization of Giorgi and Chameides (1985).

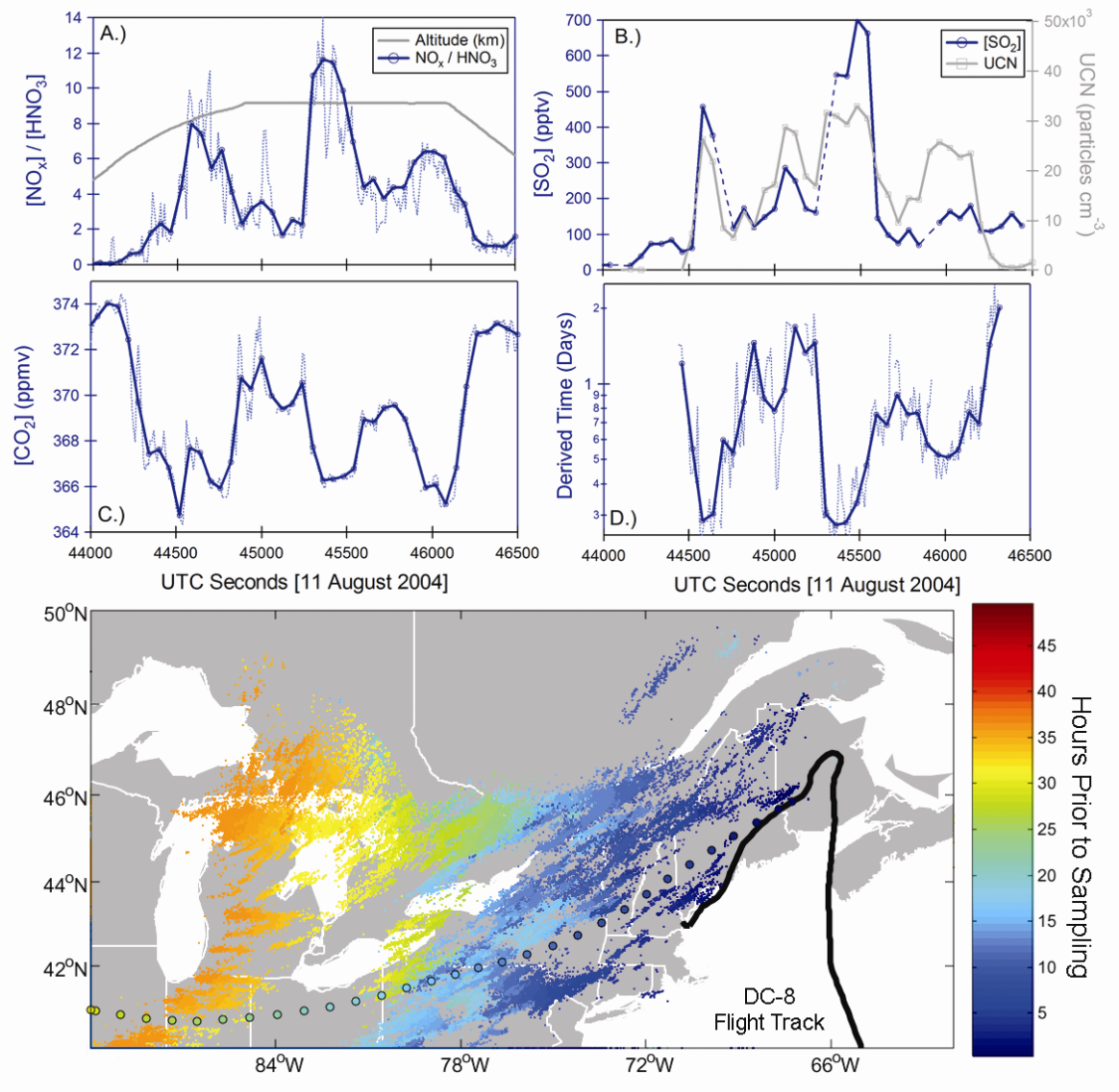

Figure 3: *top panel* Time series of measurements taken in the vicinity of recent convective activity on 11 August 2004 between 5 and 9 km. Panel A suggests the sampling of a series of fresh convective plumes, indicated by a sharp increase in the NO_x/HNO_3 ratio. Panels B & C depict coincident enhancements in SO_2 and UCN ($3nm < D_p > 10nm$) and coincident sharp drops in CO_2, indicative of the convective lofting of boundary layer air depleted in CO_2. The derived time since the sampled air-mass had been influenced by convection is shown in Panel D. *bottom panel* NLDN lightning hits (small dots) on the 10th and 11th of August. The color-code represents the time of the hit (hours) prior to aircraft sampling. The DC-8 sampling location corresponding to measurements shown in Figure 1 is located on the Maine – New Brunswick border [46ºN 67ºW]. The two day back trajectory [•] (initialized at the point of the second convective plume shown in Panel A) is also color-coded by time prior to DC-8 sampling (dots with black edges).

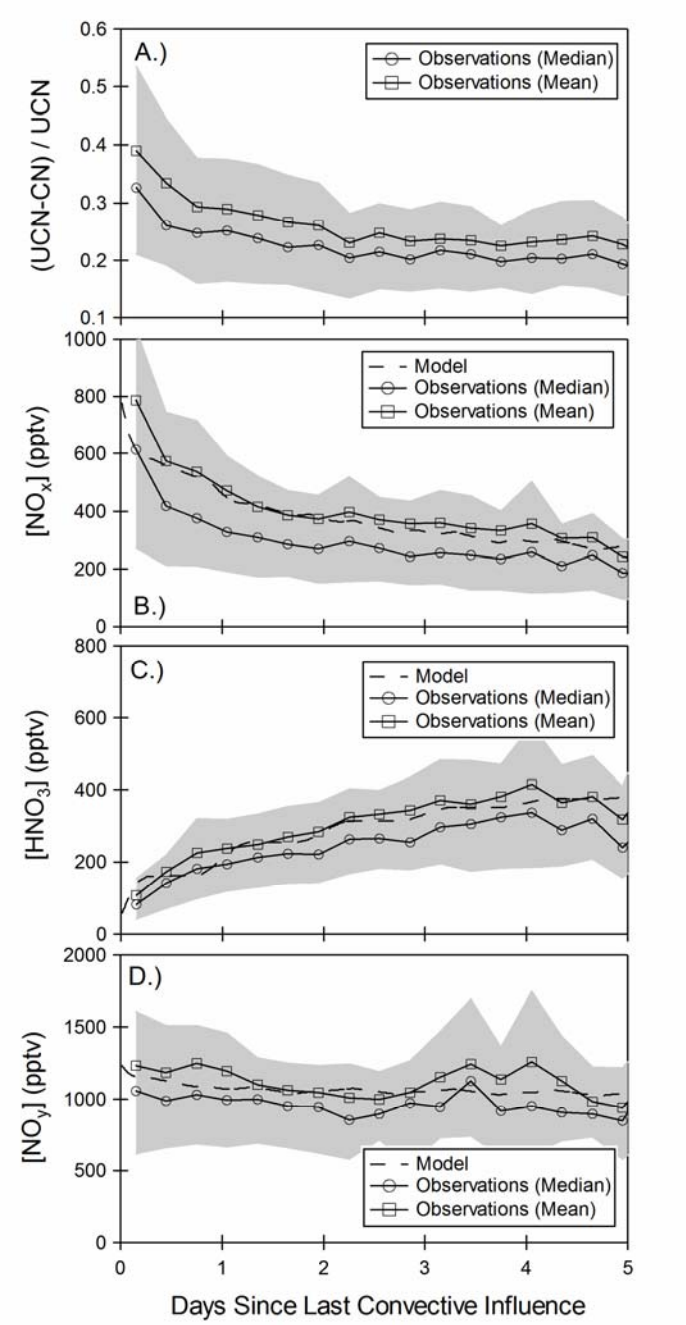

Figure 4: Observations of the fraction of ultra-fine condensation nuclei [number density of aerosol (3-10 nm) / total aerosol number density] (Panel A), NO_x (Panel B), HNO_3 (Panel C) and NO_y (Panel D) as a function of modeled time since convective influence. The mean (-□-) and median (-○-) of the observations, within 8 hour bins, is shown along with interquartile range (shaded region). Results from the time-dependent box model, initialized at 10 km and 12PM, are shown with dashed lines for the gas phase species (B-D).

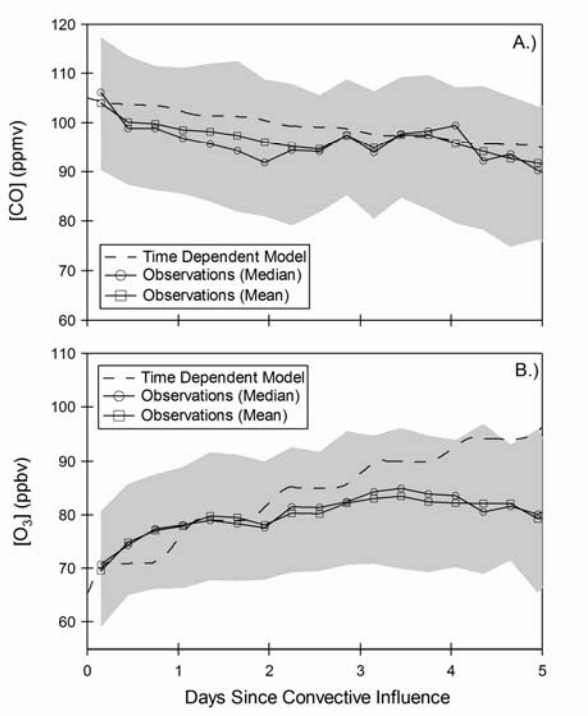

Figure 5: Observations of CO (Panel A) and Ozone (Panel B) as a function of modeled time since cloud processing in the UT. The mean (-□-) and median (-○-) of the observations, within 8 hour bins, is shown along with the interquartile range (shaded region). Results from the time-dependent box model, initialized at 10 km and 12PM, are shown with dashed lines.

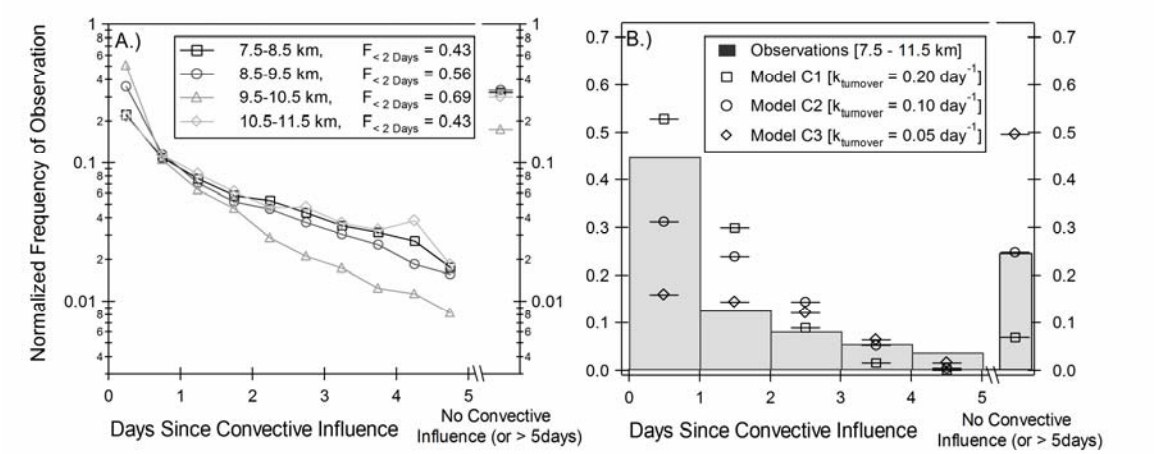

Figure 6: *left panel* Normalized frequency distribution in the time since convective influence, as calculated from observations of the NO_x to HNO_3 ratio made during the summer of 2004. Calculations are separated into 1 km altitude bins (ranging from 7.5-11.5 km). The fraction of air that had been influenced by convection within the past two days ($f_{< 2\ days}$) is included in the figure legend. *right panel* Comparison of observed frequency distribution (7.5-11.5 km) with various modeled representations of the convective turnover rate.

References and Notes:

1. R. B. Chatfield, P. J. Crutzen, *J. Geophys. Res.* **89**, 7111 (1984).
2. R. R. Dickerson *et al.*, *Science* **235**, 460 (1987).
3. K. E. Pickering, R. R. Dickerson, G. J. Huffman, J. F. Boatman, A. Schanot, *J. Geophys. Res.* **93**, 759 (1988).
4. A. M. Thompson *et al.*, *J. Geophys. Res.* **99**, 18703 (1994).
5. W. J. Collins, R. G. Derwent, C. E. Johnson, D. S. Stevenson, *Q.J.R. Meteorol. Soc.* **128**, 991 (2002).
6. J. E. Dye *et al.*, *J. Geophys. Res.* **105**, 10023 (2000).
7. S. A. Rutledge, R. A. Houze, M. I. Biggerstaff, T. Matejka, *Mon. Weather Rev.* **116**, 1409 (1988).
8. H. Huntrieser, H. Schlager, C. Feigl, H. Holler, *J. Geophys. Res.* **103**, 28247 (1998).
9. B. Ridley *et al.*, *J. Geophys. Res.* **109** (2004).
10. "Scientific assessment of ozone depletion" (World Meteorological Organization, Geneva 1995).
11. L. Jaegle, L. Steinberger, R. V. Martin, K. Chance, *Faraday Discuss.* **130**, 1 (2005).
12. A. J. DeCaria, K. E. Pickering, G. L. Stenchikov, L. E. Ott, *J. Geophys. Res.* **110** (2005).
13. J. Lelieveld, P. J. Crutzen, *Science* **264**, 1759 (1994).
14. M. G. Lawrence, R. von Kuhlmann, M. Salzmann, P. J. Rasch, *Geophys. Res. Let.* **30** (2003).
15. M. Gauss *et al.*, *J. Geophys. Res.* **108** (2003).
16. I. Folkins, K. K. Kelly, E. M. Weinstock, *J. Geophys. Res.* **107** (2002).
17. M. T. Chahine, *Nature* **359**, 373 (1992).
18. J. A. Thornton, P. J. Wooldridge, R. C. Cohen, *Anal. Chem.* **72**, 528 (2000).
19. P. A. Cleary, P. J. Wooldridge, R. C. Cohen, *Applied Optics* **41**, 6950 (2002).
20. R. W. Talbot *et al.*, *Geophys. Res. Let.* **26**, 3057 (1999).
21. J. D. Crounse, K. A. McKinney, A. J. Kwan, P. O. Wennberg, *In Press Anal. Chem.* (2006).
22. I. C. Faloona *et al.*, *J. Atmos. Chem.* **47**, 139 (2004).
23. M. A. Avery, *Submitted J. Oceanic and Atmos.Tech.* (2006).
24. A. D. Clarke *et al.*, *J. Geophys. Res.* **109** (2004).
25. R. E. Shetter, M. Muller, *J. Geophys. Res.* **104**, 5647 (1999).
26. G. W. Sachse, G. F. Hill, L. O. Wade, M. G. Perry, *J. Geophys. Res.* **92**, 2071 (1987).
27. S. A. Vay *et al.*, *J. Geophys. Res.* **104**, 5663 (1999).
28. H. B. Singh, W. H. Brune, J. H. Crawford, D. J. Jacob, *Submitted J. Geophys. Res.* (2006).
29. R. Sander, "Compilation of Henry's Law Constants for Inorganic and Organic Species of Potential Importance in Environmental Chemistry (Version 3)" (Mainz, Germany 1999).
30. M. J. Prather, D. J. Jacob, *Geophys. Res. Let.* **24**, 3189 (1997).
31. L. Jaegle *et al.*, *Geophys. Res. Let.* **25**, 1705 (1998).

32. Y. Wang *et al.*, *Geophys. Res. Let.* **27**, 369 (2000).
33. D. S. Cohan, M. G. Schultz, D. J. Jacob, B. G. Heikes, D. R. Blake, *J. Geophys. Res.* **104**, 5717 (1999).
34. S. Smyth *et al.*, *J. Geophys. Res.* **101**, 1743 (1996).
35. S. A. McKeen, S. C. Liu, *Geophys. Res. Let.* **20**, 2363 (1993).
36. F. J. Dentener, P. J. Crutzen, *J. Geophys. Res.* **98**, 7149 (1993).
37. F. Giorgi, W. L. Chameides, *J. Geophys. Res.* **90**, 7872 (1985).
38. D. D. Davis *et al.*, *J. Geophys. Res.* **101**, 2111 (1996).
39. D. J. Jacob *et al.*, *J. Geophys. Res.* **101**, 24235 (1996).
40. R. B. Chatfield, *Geophys. Res. Let.* **21**, 2705 (1994).
41. A. Tabazadeh *et al.*, *Geophys. Res. Let.* **25**, 4185 (1998).
42. D. A. Hauglustaine, B. A. Ridley, S. Solomon, P. G. Hess, S. Madronich, *Geophys. Res. Let.* **23**, 2609 (1996).
43. A. D. Clarke *et al.*, *J. Geophys. Res.* **104**, 5735 (1999).
44. H. Huntrieser *et al.*, *J. Geophys. Res.* **107** (2002).
45. H. E. Fuelberg, M. J. Porter, C. M. Kiley, D. Morse, *Submitted J. Geophys. Res.* (2006).
46. J. A. Snow *et al.*, *Submitted J. of Geophys. Res.* (2006).
47. R. C. Hudman *et al.*, *Accepted J. Geophys. Res.* (2006).
48. O. R. Cooper *et al.*, *Accepted J. of Geophys. Res.* (2006).
49. E. A. Ray *et al.*, *J. Geophys. Res.* **109** (2004).
50. T. Hauf, P. Schulte, R. Alheit, H. Schlager, *J. Geophys. Res.* **100**, 22957 (1995).
51. Net ΔOzone of 0 nmol mol^{-1} day^{-1} could be achieved if the air parcel: i.) subsided to where H_2O abundances are large enough to provide a sink of O_3 through O^1D that balanced production from $NO+HO_2$ (~6 km), ii.) entrained air containing lower O_3 mixing ratios or iii.) contained additional O_3 loss terms beyond NO_x, HO_x, H_2O (via O^1D removal). To match the deviation between the model and measurement, we would require an additional 2-3 nmol mol^{-1} day^{-1} of chemical ozone loss. In order for mixing to explain the deviation, air of lower O_3 would need to be mixed into the air parcel. As shown in Fig. 5b, the only air in the UT containing significantly less O_3 is that pumped directly from the PBL. While mixing fresh and aged outflow could help to explain the discrepancy in O_3, it is inconsistent with the observed decay in CO at long time (2-5 days).
52. D. Rind, J. Lerner, *J. Geophys. Res.* **101**, 12667 (1996).
53. G. L. Mullendore, D. R. Durran, J. R. Holton, *J. Geophys. Res.* **110** (2005).
54. K. E. Pickering, Y. S. Wang, W. K. Tao, C. Price, J. F. Muller, *J. Geophys. Res.* **103**, 31203 (1998).
55. A. M. Thompson *et al.*, *Submitted J. Geophys. Res.* (2006).
56. W. B. Rossow. (http://isccp.giss.nasa.gov/index.html, published online 2006).
57. J. Dibb, E. Scheuer, R. Talbot, M. Avery, *Submitted J. Geophys. Res.* (2006).
58. Fuelberg et al. use 10-day back trajectories to National Weather Service Global Forecast System (GFS) derived convection and National Lightning Detection Network (NLDN) measured lightning strikes to assess the fraction of time that the DC-8 sampled either convection or lightning influenced air. Using the GFS statistics, Fuelberg et al. calculate that 63% of the sampled air on INTEX-NA had encountered convection and ~57% had been influenced by lightning during the

past 2 days. In Fuelberg et al., the authors determine that when considering the entire INTEX-NA sampling domain (both in space and time), convection was present in 12.5% of the grid points. This is substantially smaller than the percent of observations within 6 hours of convection (21.4%), suggesting that the DC-8 had a positive bias toward sampling fresh convection. This bias is reflected in the sharp drop in population between day 1 and 2 as shown in Fig. 6a. Correcting for this bias has little effect on our assessment of the fraction of air less than 2 days old, lowering our results from 0.43, 0.56, 0.69, and 0.43 to 0.38, 0.50, 0.62, and 0.39 at 8, 9, 10, and 11 km respectively.

59. I. Folkins, R. V. Martin, *Journal of the Atmospheric Sciences* **62**, 1560 (2005).

60. The authors thank the flight and ground crews of the NASA DC-8 Aircraft and the entire INTEX-NA science team for their contributions during the 2004 intensive field campaign. We thank A.M. Thompson, I. Folkins, M.G. Lawrence and D. Allen for helpful discussions, T. Kucsera for help with the GEOS-4 calculations and W.H. Brune and X. Ren for OH and HO_2 data. NLDN data was collected by Vaisalia-Thunderstorm and provided to the INTEX Science Team by the Global Hydrology Resource Center (GHRC) at NASA Marshall Space Flight Center (MSFC). Work at U.C. Berkeley was supported under NASA grants NNG05GH196 and NAG5-13668. The INTEX-NA field program was supported by the NASA-ESE Tropospheric Chemistry Program.

Supplemental Online Information

1. INTEX-NA Experiment Description and Instrument Descriptions

The Intercontinental Chemical Transport Experiment – North America (INTEX-NA) took place between 1 July and 14 August 2004. Research flights were conducted out of Dryden Flight Research Center (Edwards AFB, CA), Mid-America Airfield (Mascoutah, IL); and PEASE International Trade-Port (Portsmouth, NH). Figure S1 depicts the vertical and horizontal extent of research flights conducted aboard the NASA DC-8 during INTEX-NA (*1*). DC-8 flight tracks are shown in the left panel of Figure 1 and the number of samples (10 second averaging time) in 1km vertical bins are shown in the right panel. *In situ* observations relevant to this study include; NO_2, HNO_3, OH, O_3, CO, CO_2, SO_2 and Ultra-fine Condensation Nuclei (UCN). Table S1 describes the detection threshold, uncertainty and time response for each measurement used in this analysis.

NO_2 LIF Instrument The NO_2 instrument flown aboard the DC-8 was described in detail by Thornton et al. (*2*), with specifics of the jet-expansion described by Cleary et al. (*3*). Briefly, NO_2 fluorescence is detected at 1Hz following excitation of a specific jet-cooled rovibronic transition in NO_2 at 585 nm. Red-shifted fluorescence is imaged at 90º onto an air cooled photomultiplier tube that is both optically and temporally filtered to remove laser scatter. NO_2 mixing ratios are calculated directly from fluorescence counts following calibration to NO_2 gas standards and measurements of the instrument zero from compressed air mixtures containing zero NO_2. Selectivity to NO_2 is demonstrated by tuning on and off of a specific NO_2 resonance, where the difference in observed fluorescence at the two different frequencies is attributed solely to NO_2. We calculate a

NO_2 detection threshold of 8 pptv in 10 seconds at the surface and 25 pptv in 10 seconds at the aircraft ceiling (12.5 km).

2. 0-D Time Dependent Model

The chemical evolution of convective outflow was modeled using a 0-D time dependent model. The model was initialized with chemical conditions, altitudes and detrainment times consistent with observations of fresh convection made during INTEX-NA. As time propagates in the model, we calculate the production and loss of O_3, CO, NO, NO_2, NO_3, N_2O_5, PAN, HO_2NO_2, HNO_3, OH, HO_2, RO_2, H_2O_2, CH_3OOH, H_2CO and C1-C6 Hydrocarbons for 20 days following cloud detrainment. The conversion of NO_x to HNO_3 in the outflow region is used as an indicator of time since convection. Figure S2 depicts the results of a single run initialized at 10km with a noon detrainment time. Initial conditions correspond to $[NO_x]_i = 800$ pptv, $[O_3]_i = 65$ ppbv and $[CO]_i = 105$ ppbv. Rapid conversion of NO_x to HNO_3 is observed during the first few days as the system approaches steady-state. In this analysis we assume: i.) HNO_3 is scavenged with unit efficiency in deep convection, ii.) $\gamma_{N2O5} = 0.01$ and iii.) HNO_3 is not scavenged by aerosols (or rain) following injection into the UT. All kinetic rates used in this analysis were taken from the NASA JPL Chemical Kinetics and Photochemical Data for Use in Atmospheric Studies, Evaluation Number 14 (*4*).

2.1 Treatment of OH and HO_2

The calculated time since convective detrainment is directly coupled to the HO_x budget through the daytime NO_x sink to HNO_3 via reaction with OH. As in other model

descriptions of the UT during INTEX-NA (*5, 6*), our unconstrained model over-estimates OH by nearly a factor of two in the UT and under-estimates HO_2 by a similar amount. Due to the direct dependence of our timing indicator on HO_x, we constrain the mixing ratios of OH and HO_2 to the observed values as a function of NO_x and altitude. Figure S3 depicts the modeled mixing ratios of OH and HO_2 (lines), constrained to the observations (dots), as a function of NO_x and SZA at 10km. The observed OH is a strong function of NO_x, while observations of HO_2 remain insensitive to NO_x. Constraints for OH and HO_2 were derived independently for each 1km altitude bin. Constraining OH and HO_2 to the observations increases the time required for the NO_x-HNO_3 system to reach steady-state (by slowing the rate of OH + NO_2) and enhances the modeled O_3 production in the outflow region (by speeding up the rate of HO_2+NO).

2.2 Calculation of Time since Convection

The time since a sampled air-mass had been cloud processed is calculated by applying the mapping of time to NO_x/ HNO_3 derived in the box model to the observed NO_x to HNO_3 ratio. Figure S4 depicts the best-fit relation between the modeled NO_x to HNO_3 ratio and time since cloud processing at 10km. This function is calculated at 1km increments from 6-12km and applied to the measured NO_x to HNO_3 ratio.

2.3 Model Assumptions and Uncertainty

In order to access the uncertainty in the calculated time, we ran the time-dependent model under various different conditions encountered during INTEX-NA (e.g. $[NO_x]_i$ (0.2-3.0 ppbv), $[O_3]_i$ (40-100 ppbv), $[CO]_i$ (80-150 ppbv), detrainment time (noon, 4PM,

midnight), altitude (6-12km) and time of year (June-September). As illustrated in figure S4, the NO_x to HNO_3 ratio has good resolution (i.e. large rate of change per unit time) during the first five days following convection. Beyond five days small changes in NO_x/HNO_3 correspond to larger changes in the derived time. From the variance in the calculated time of individual model runs, we estimate the uncertainty in our modeled time to be ±6 hours at 1 day, ±12 hours at 2 days and ±1 day at 4 days. In addition, the INTEX-NA sampling domain did not permit frequent measurement of aged convection (>5 days). For these reasons we limit our analysis to the first five days following convection.

2.4 Treatment of Mixing

The mixing rate was determined by iterating the model until we had closure between the observed and modeled time evolution of a suite of long-lived species (e.g. CO, CH_4, CH_3OH and others). The modeled time rate of change of species X is determined as:

$$\frac{d[X]}{dt} = P(X) - L(X) - k_{dilution}\left([X] - [X]_{Background}\right)$$

where P(X) represents the chemical production of species X, L(X) represents the chemical loss of species X and $k_{dilution}$ is the mixing rate of the convective plume with background UT. We find this mixing term to be on average 0.05 ± 0.02 day^{-1}. That is, after 5 days, the plume still has 75% of its original contents. While individual convective plumes may mix faster (or slower) that this, the aggregate mixing rate of all the sampled plumes can be described by this rate. This rate supports the conclusion that over the course of 5 days, the convective plume remains relatively isolated from the background

UT. Background mixing ratios used in the dilution calculation were taken as the mean observed UT mixing ratios outside of fresh convective plumes.

Due to subsidence of convectively lofted air parcels following injection, our calculated time represents a lower bound for age as the chemical clock speeds up (due to NO_x repartitioning) as the parcel descends in altitude. However, this is a relatively small effect as calculated subsidence rates are approximately 35 hPa day^{-1} (*7*).

3.0 Comparison of Chemical and Meteorological Convective Influence Calculations

The results presented here provide a chemical constraint on the rate at which the UT over the continental US is influenced by convection during summer. In addition to the meteorological analysis of Fuelberg et al., presented in this manuscript, Thompson et al. assessed the effects of convection on the O_3 budget in the UT, over eastern North America, during the summer of 2004. Using results from the INTEX Ozone Sonde Network Study (IONS), the authors conclude that 10-15% (lower-limit) of the below tropopause O_3 can be attributed to the interaction of regional pollution with convection and lightning (*8*).

The INTEX-NA sampling period (June-August) and region (Eastern North America) is characterized by intense lightning activity. Cooper et al. calculated that 13% of the global annual lightning NO_x emissions occurred between 108º W – 18 º E and 18 º -72º N the between June 21 and August 15, 2004 (*9*). In terms of lightning flash counts, Hudman et al., conclude that 2004 was typical (within 20% of the mean) of the past 5

years (*6*). Persistent frontal passages prevented the formation of stagnant high pressure systems, typically observed during the summer over the northeastern United States (*10*). These frequent passages led to both record low temperatures and number of O_3 exceedances in the northeast (*11*). In contrast UT/LS O_3, as observed from the IONS network, was comparable to the climatology (*11*).

4.0 Measurement Uncertainties

In this analysis we calculate NO_x from observations of NO_2, O_3, HO_2 and photolysis rates measured directly on the DC-8. NO was measured directly on the DC-8 via a commercial grade chemiluminescence detector. The sensitivity of the chemiluminescence instrument (detection threshold > 50 pptv) and long integration time (1 minute) prohibited its use in these calculations. NO was calculated from steady-state using the following equation:

$$[NO]_{Steady-State} = \frac{J_{NO_2}[NO_2]}{k_{NO+O_3}[O_3] + k_{NO+HO_2}[HO_2]}$$

We calculate the accuracy of the derived NO to be better than ± 30% based on the propagation of the individual errors used on the calculation. Observations of Nitrogen Dioxide, Ozone and JNO_2 made during the INTEX-NA campaign were compared directly with measurements made aboard the NOAA WP-3D during a series of in-flight comparisons. During these experiments the principal individual components (NO_2, O_3 and JNO_2) showed agreement to within their stated instrumental uncertainty.

In Figure S6 we compare the measured NO_x (using the chemiluminescence and the Laser Induced Fluorescence measurements) and NO_x calculated from steady-state for the entire INTEX-NA campaign. The steady-state NO_x agrees with the measured NO_x to within the calculated uncertainty when averaged to 1-minute and divided into 1km vertical bins. The observed upper tropospheric NO_x concentrations during INTEX-NA are on average much higher than previous reported on intensive aircraft field campaigns over North America. During the SUCCESS campaign, Jaegle et al. report mean NO concentrations of 0.030 ± 0.022 ppbv and 0.061 ± 0.045 ppbv, for the altitude ranges of 8-10 km and 10-12 km, respectively (*12*). However, it must be noted that the scientific objective of SUCCESS was the sampling of aircraft exhaust and contrails, thus the values reported in Jaegle et al., were filtered to exclude fresh aircraft exhaust (CO_2 > 368 ppmv and NO > 300 pptv). Crawford et al., report mean NO concentrations of 0.1 ppbv for observations made between 6-12 km during the SONEX campaign during the fall of 1997 over the North Eastern United States and the North Atlantic (*13*). Neither of these studies provides a direct comparison to the INTEX-NA data-set as SUCCESS was conducted in the spring and SONEX in the fall, while peak lightning and convection occurs over the continental North America during summer. The best comparison comes from NO_x measured aboard a commercial passenger aircraft during the NOXAR program between 1995 and 1997. Brunner et al. report a mean UT NO_x concentration of 0.4 ppbv during June, July and August over North America (*14*). As seen in Figure S6, our observations during the summer of 2004 are consistent with this.

We use the Caltech CIMS HNO_3 due to its fast time response (5 seconds as compared to 105 seconds for the UNH Mist Chamber Technique) and the UNH MC results when the fast HNO_3 was unavailable. To account for the systematic bias between the two observations in the UT ($[HNO_3]_{UNH} = 0.6 \times [HNO_3]_{Caltech}$), we scale both the CIMS and MC observations to split the difference between the two measurements (i.e. we increase $[HNO_3]_{UNH}$ by 20% and decrease $[HNO_3]_{CIT}$ by 20%).

Due to the observed systematic bias, the choice of which HNO_3 measurement to use in the analysis has the potential to complicate our conclusions. To address these effects we have conducted the analysis using Nitric Acid as measured from: i.) the Mist Chamber – Ion Chromatography Instrument, ii.) the Chemical Ionization Mass Spectrometer and iii.) the scaled difference between the two techniques. The results are compared in Figures S7 and S8. Figure S7 shows the normalized frequency distribution in the time since convective influence, as calculated from observations of the NO_x to HNO_3 ratio made during the summer of 2004. Figure S8 depicts the fraction of air that had been influenced by convection within the past two days ($f_{< 2\ days}$) as a function of altitude. Calculations derived from the Mist Chamber – Ion Chromatography Instrument result in a higher fraction of convectively influenced air when compared with calculations made using measurements from the CIMS instrument. When compared with the results shown in Figure 6B of the manuscript, on which our conclusions regarding the convective overturn rate are drawn from, calculations using either the CIMS, MC-IC or the scaled difference result in a convective overturn rate between 0.1 and 0.2 day^{-1}.

2. Supplemental Figures

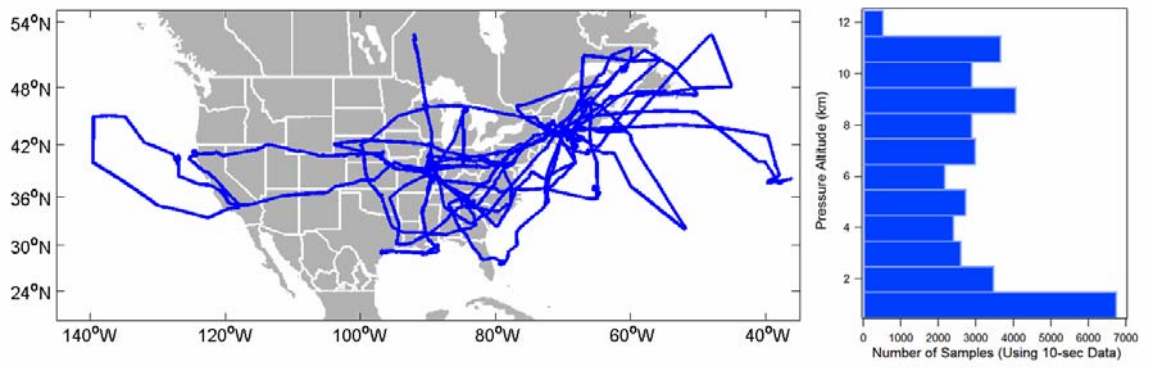

Figure S1: *left panel* INTEX-NA flight tracks made between 1 July 2004 and 14 August 2004 aboard the NASA DC-8. *right panel* Number of samples (using 10-sec averaged data) within 1km altitude bins between 0-12 km during the entire campaign.

1

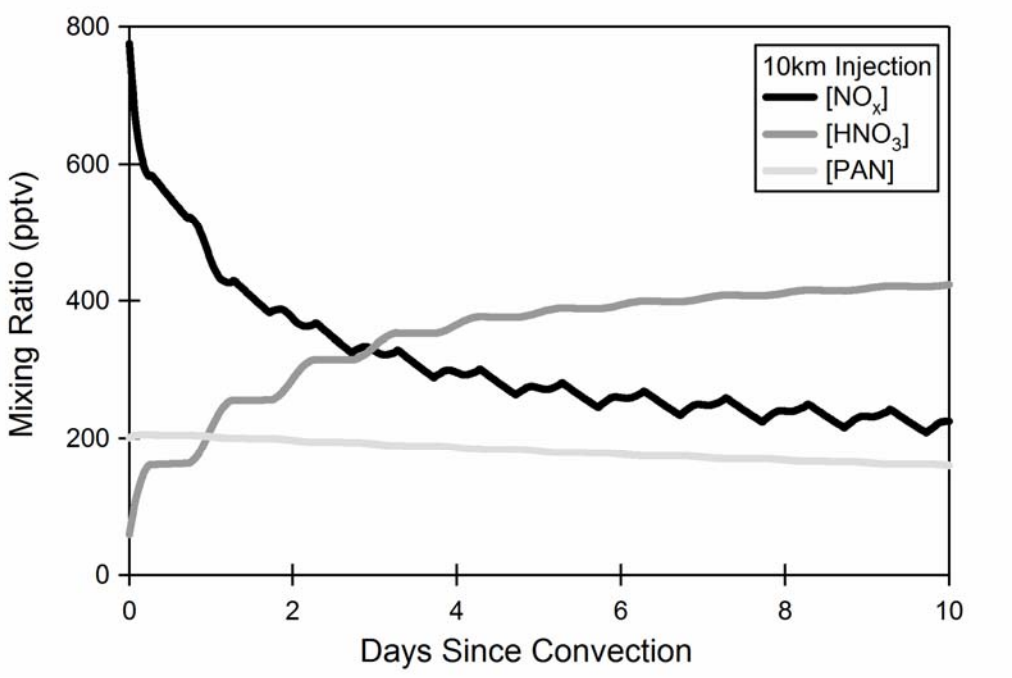

2

3 **Figure S2:** Time-dependent model illustrating the conversion of NO_x to Nitric Acid in
4 the days subsequent to a cloud processing event occurring at 10km. The above model
5 was initialized at 12PM local time at 30ºN in August using $[NO_x]_i$ = 800 pptv, $[CO]_i$ =
6 105 ppbv at $[O_3]_i$ = 65 ppbv.

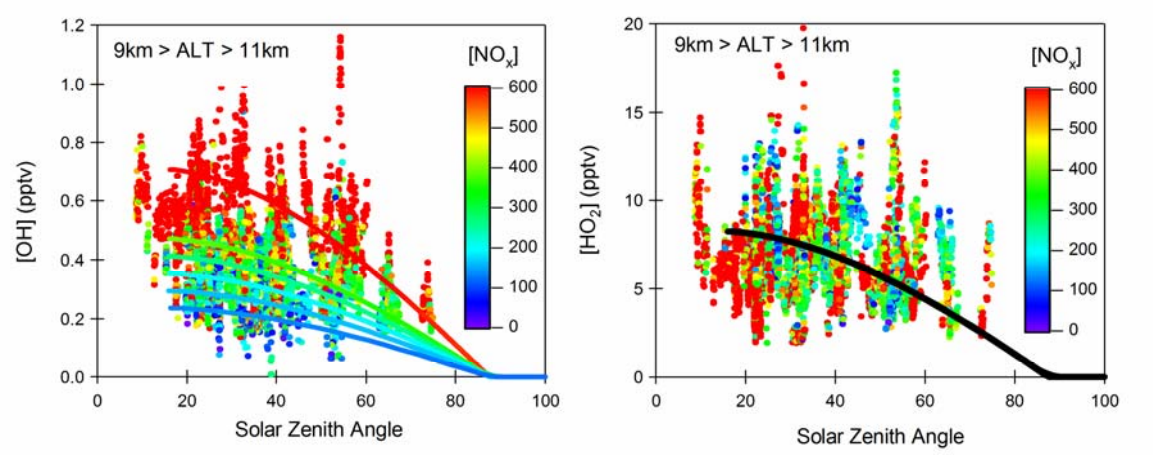

Figure S3: Model representation of OH (left panel) and HO_2 (right panel) as a function of SZA and $[NO_x]$. Model results (solid lines) are shown on top of the *in situ* observations (dots). The model was initialized at noon at 10km with $[NO_x]_i$ = 800 pptv, $[CO]_i$ = 105 ppbv at $[O_3]_i$ = 65 ppbv. Observations shown were taken aboard the DC-8 between 9 and 11 km.

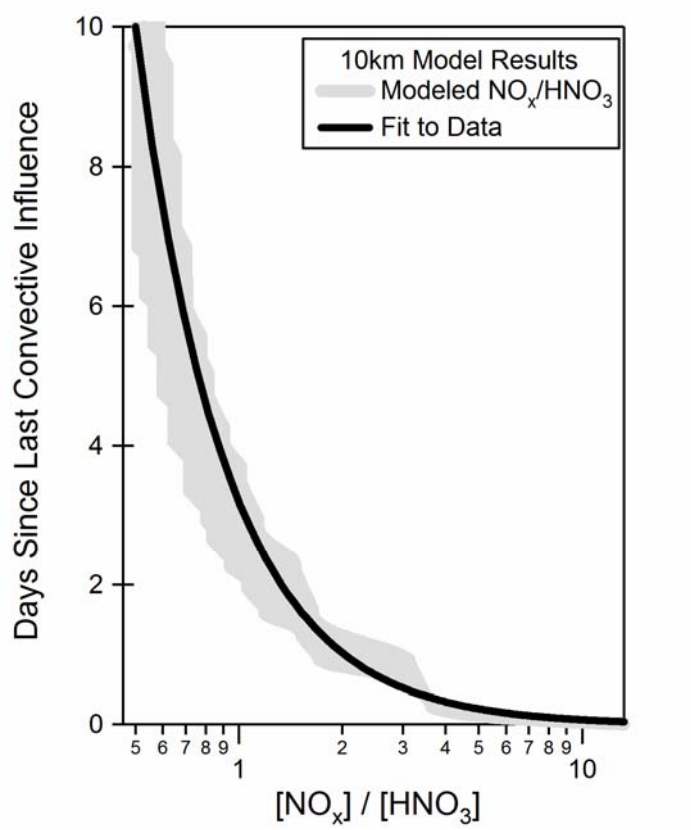

Figure S4: Observed NO_x to HNO_3 ratios are converted to a time since last convective influence using the best fit equation relating the NO_x/HNO_3 ratio to time as calculated using the time-dependent model in 1km altitude bins from 7.5-11.5 km. The above equation is valid for pressure altitudes between 9.5 and 10.5 km.

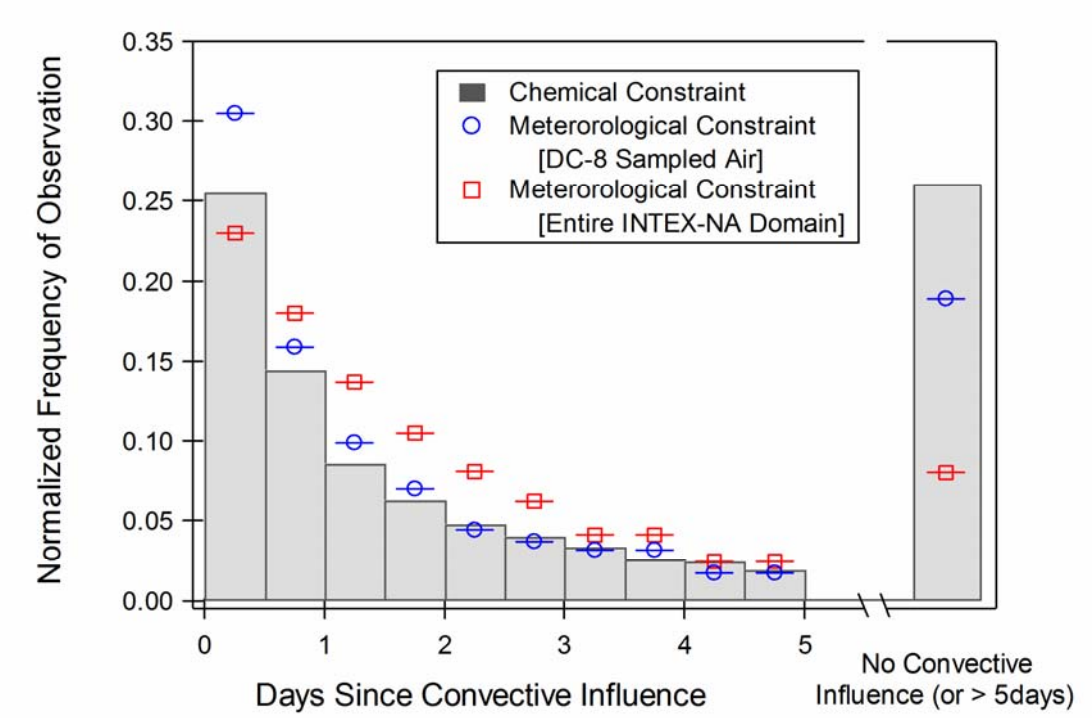

Figure S5: Comparison of chemical (grey bars) and meteorological constraints (-○-, -□-) on convective influence during INTEX-NA. Convective influence on air *sampled* by the DC-8 is shown with blue circles (-○-), while convective influence on the entire INTEX-NA domain is shown with red squares (-□-).

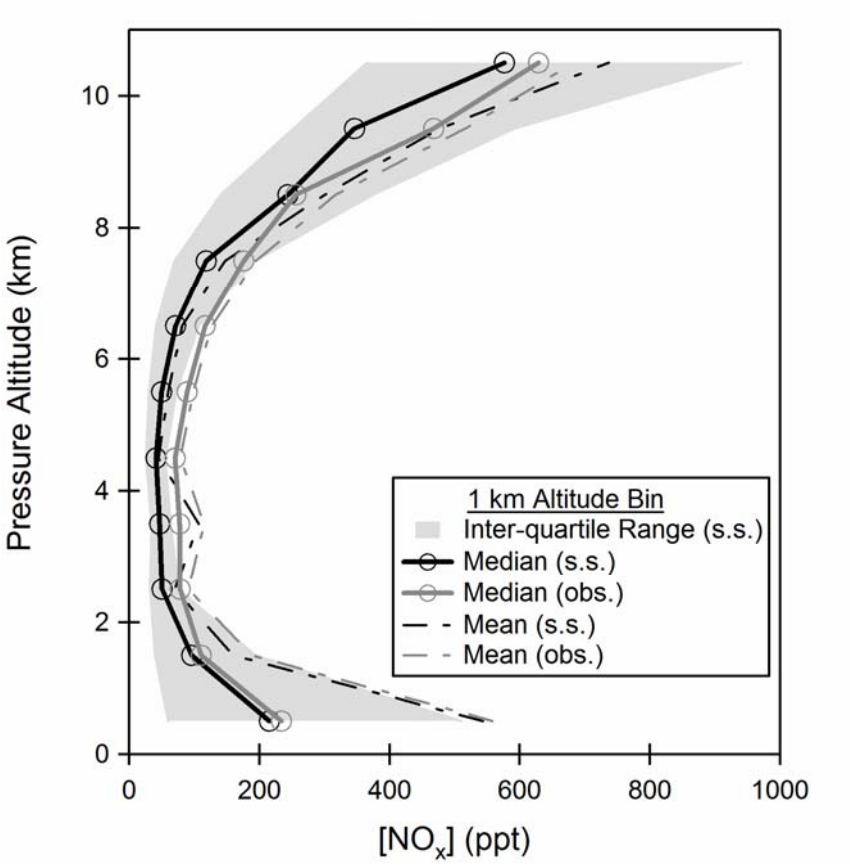

Figure S6: Comparison of observed (grey lines) and steady-state (black lines) NO_x for the entire INTEX-NA field campaign. The shaded region represents the interquartile range of the calculated NO_x.

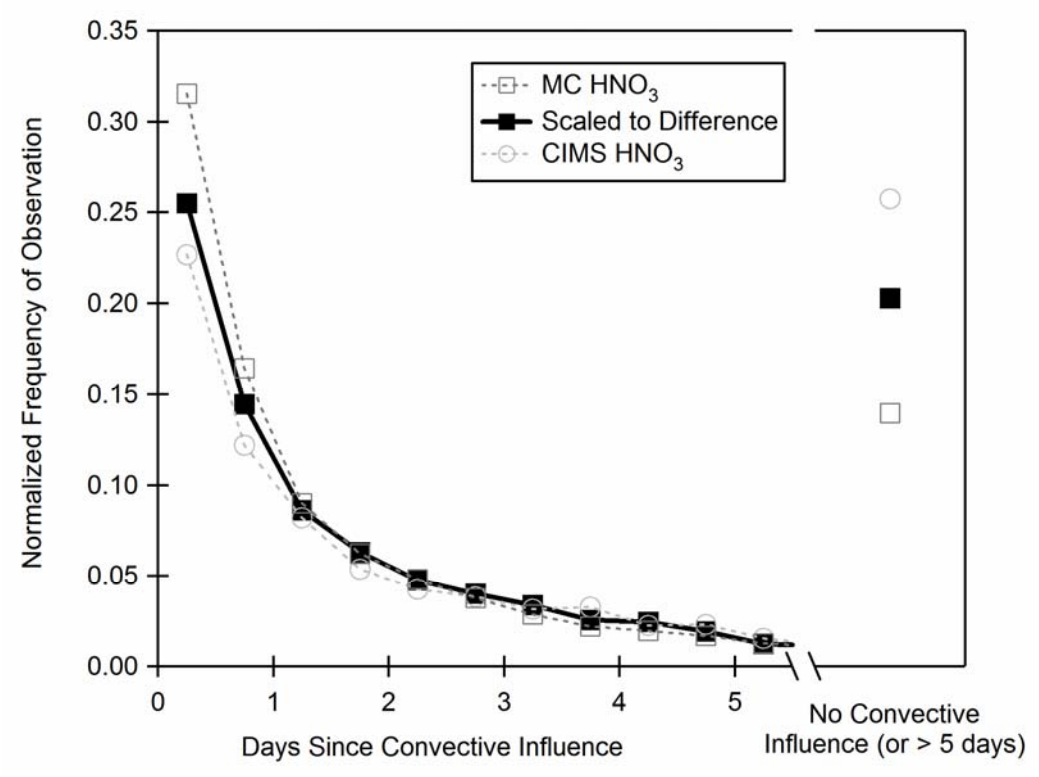

Figure S7: Normalized frequency distribution in the time since convective influence, as calculated from observations of the NO_x to HNO_3 ratio made during the summer of 2004. Calculations were conducted using Nitric Acid as measured from: i.) the Mist Chamber – Ion Chromatography Instrument (-□-), the Chemical Ionization Mass Spectrometer (-○-) and the scaled difference (-■-).

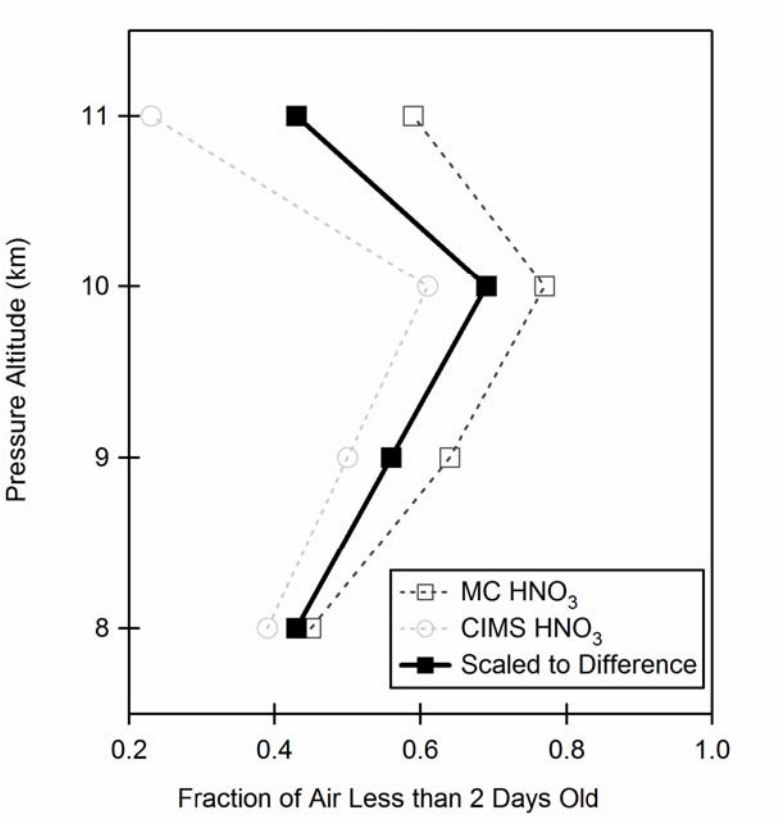

Figure S8: Fraction of air that had been influenced by convection within the past two days ($f_{<2\ days}$) as a function of altitude. Calculations were conducted using Nitric Acid as measured from: i.) the Mist Chamber – Ion Chromatography Instrument (-□-), the Chemical Ionization Mass Spectrometer (-○-) and the scaled difference (-■-).

Species	Measurement Technique	Detection Threshold	Accuracy	Time Response	Reference
NO_2	LIF[1]	8 pptv / 10 sec	± 10% 1σ	1 Hz	(*2, 3*)
HNO_3	CIMS[3]	10 pptv / 0.5s	± 30%	0.5s sample every 5s	(*15*)
	Mist Chamber – IC[4]	5 pptv / 105 sec		105 sec	(*16*)
OH	LIF[1]	0.01 pptv	± 32% 2σ - 1 min	20 sec	(*17*)
O_3	Chemiluminescence	Precision = ±0.8pptv, ±1% of reading	± 2 ppbv, ±3%	1 Hz	(*18*)
CO	IR-Absorption	Precision = ±1ppbv, ±1.5% of reading	± 1.4 ppbv, ± 2.6% 2σ	1 Hz	(*19*)
CO_2	IR-Absorption	Precision < 0.07 ppmv	± 0.25 ppmv	1 Hz	(*20*)
UCN	TSI CN counter[5]	± 10%	± 10%	1 Hz	(*21*)
J_{NO2}	Actnic Flux Spectroradiometer	4.1×10^{-7} Precision = ±4.5%	± 8%	1 Hz	(*22*)

[1]LIF – Laser Induced Fluorescence
NO_2 detection threshold is 8 pptv / 10 sec at 760 Torr (ground) and 20 pptv / 10 sec at 200 Torr (10 km)
[3]CIMS – Chemical Ionization Mass Spectrometry
[4]IC – Ion Chromatography
[5]UCN (Ultra-fine Condensation Nuclei) was obtained by the difference of the UCN (D_p>3nm, TSI 3025) and CN (D_P>10nm, TSI 3010) Condensation Nuclei (CN) instruments.

Table S1: Detection thresholds, measurement uncertainty and time response of the *in situ* measurements used in this study. (Note: ppmv = μmol mol^{-1}, ppbv = nmol mol^{-1} and pptv = pmol mol^{-1})

References and Notes:

1. H. B. Singh, W. H. Brune, J. H. Crawford, D. J. Jacob, *Submitted J. Geophys. Res.* (2006).
2. J. A. Thornton, P. J. Wooldridge, R. C. Cohen, *Anal. Chem.* **72**, 528 (2000).
3. P. A. Cleary, P. J. Wooldridge, R. C. Cohen, *Applied Optics* **41**, 6950 (2002).
4. S. P. Sander *et al.*, "Chemical Kinetics and Photochemical Data for Use in Atmospheric Studies, Evaluation Number 14" (National Aeronautics and Space Administration, Jet Propulsion Laboratory, California Institute of Technology, Pasadena, CA 2003).
5. X. R. Ren *et al.*, *Submitted J. Geophys. Res.* (2006).
6. R. C. Hudman *et al.*, *Accepted J. Geophys. Res.* (2006).
7. E. P. Salathe, D. L. Hartmann, *Journal of Climate* **10**, 2533 (1997).
8. A. M. Thompson *et al.*, *Submitted J. Geophys. Res.* (2006).
9. O. R. Cooper *et al.*, *Accepted J. of Geophys. Res.* (2006).
10. H. E. Fuelberg, M. J. Porter, C. M. Kiley, D. Morse, *Submitted J. Geophys. Res.* (2006).
11. A. M. Thompson *et al.*, *Submitted J. Geophys. Res.* (2006).
12. L. Jaegle *et al.*, *Geophys. Res. Let.* **25**, 1705 (1998).
13. J. Crawford *et al.*, *J. Geophys. Res.* **105**, 19795 (2000).
14. D. Brunner, J. Staehelin, D. Jeker, H. Wernli, U. Schumann, *J. Geophys. Res.* **106**, 27673 (2001).
15. J. D. Crounse, K. A. McKinney, A. J. Kwan, P. O. Wennberg, *In Press Anal. Chem.* (2006).
16. R. W. Talbot *et al.*, *J. Geophys. Res.* **102**, 28303 (1997).
17. I. C. Faloona *et al.*, *J. Atmos. Chem.* **47**, 139 (2004).
18. M. A. Avery, *Submitted J. Oceanic and Atmos.Tech.* (2006).
19. G. W. Sachse, G. F. Hill, L. O. Wade, M. G. Perry, *J. Geophys. Res.* **92**, 2071 (1987).
20. B. E. Anderson *et al.*, *J. Geophys. Res.* **101**, 1985 (1996).
21. A. D. Clarke *et al.*, *J. Geophys. Res.* **109** (2004).
22. R. E. Shetter, M. Muller, *J. Geophys. Res.* **104**, 5647 (1999).